Magnetic anisotropy and magnetocaloric effect in Gd$_2$NiMnO$_6$ thin films

Amitava Ghosh [1,*] Roumita Roy [2] R. C. Sahoo [1,3] Sachindra Nath Sarangi [4] Mithun Ghosh [5] Dipak Mazumdar [1,6]
D. Samal [4,7] P. S. Anil Kumar [5] Zakir Hossain [1] Sudipta Kanungo [2,†] and Chanchal Sow [1,‡]

[1]*Department of Physics, Indian Institute of Technology Kanpur, Kanpur 208016, India*

[2]*School of Physical Sciences, Indian Institute of Technology Goa, 403401 Goa, India*

[3]*Department of Chemical Science and Engineering, Tokyo Institute of Technology, 2-12-1 Ookayama, Meguro, Tokyo 1528552, Japan*

[4]*Institute of Physics, Bhubaneswar, Bhubaneswar 751005, India*

[5]*Department of Physics, Indian Institute of Science, Bangalore 560012, Karnataka, India*

[6]*Department of Physics, Arya Vidyapeeth College (Autonomous), Guwahati 781016, Assam, India*

[7]*Homi Bhaba National Institute, Anushaktinagar, Mumbai 400094, India*

The magnetism and magnetocaloric effect in double perovskites is an alluring area of research due to its tunable nature. In particular, the exchange interactions and local ordering of magnetic sublattices are sensitive to the chemical substitution, synthesis/growth conditions, and strain. Here we study the effect of strain on magnetism in Gd$_2$NiMnO$_6$ double perovskite thin films grown using pulsed laser deposition on SrTiO$_3$ (001) substrate. Magnetostructural study finds tensile strain to be the origin of perpendicular magnetic anisotropy in Gd$_2$NiMnO$_6$. Further, the anisotropic nature prevails in magnetocaloric effect as well. Magnetic entropy change along the in-plane direction is observed to be 21.82 J Kg^{-1} K^{-1}, which reduces to 9.84 J Kg^{-1} K^{-1} along the out-of-plane direction. Our theoretical calculation reveals a ferrimagnetic ground state of Gd$_2$NiMnO$_6$. The relative spin orientation of Ni and Mn changes from parallel configuration for strained Gd$_2$NiMnO$_6$ to antiparallel configuration for strain-relaxed Gd$_2$NiMnO$_6$.

I. INTRODUCTION

Double perovskites (DPs) with a general formula $R_2BB'O_6$, where R stands for rare-earth elements and B, B' are transition metal elements, have gained much attention due to the presence of room temperature ferromagnetism, high magnetic entropy change, and magnetodielectric coupling [1–4]. The crystal structures of DPs are mostly distorted owing to the variations in the R-site cationic radius. Goldschmidt tolerence factor defined as $t = (r_R + r_O)/\sqrt{2}(\langle r_B \rangle + r_O)$, where r_R, r_O, and $\langle r_B \rangle$ represent the radii of R, O, and average radii of the two B-site cations, respectively, is a measure of the distortion [4]. When the R site is occupied by a smaller sized cation, the structural symmetry reduces to monoclinic or orthorhombic ($t < 1$) from perfect cubic structure ($t = 1$). The origin behind such structural change is the cooperative tilting of BO_6 and $B'O_6$ octahedra, which balances the chemical pressure created by the smaller R-site cations. Such octahedral distortion alters the B-O-B' bond angle that influences the exchange interactions. Not only the bond angle but also the oxidation states and ionic radii of B and B'-site cations influence the exchange interaction. The intermixing of B and B' cations [termed as antisite disorder (ASD)] also influences the magnetic ground state of the DPs.

Among various DPs, R_2NiMnO$_6$ and R_2CoMnO$_6$ are interesting due to their complex magnetic nature, giant magnetocaloric effect, magnetodielectric effect, and multiferroic behavior [2,3,5–7]. The origin of the complex magnetism lies in the mixed valency of Mn and Ni/Co. Such mixed valency along with ASD lead to various magnetic phenomena in R_2NiMnO$_6$. In La$_2$NiMnO$_6$ (LNMO) and Nd$_2$NiMnO$_6$, mixed valency and ASD gives rise to reentrant spin-glass and exchange bias effect [3,8,9]. In polycrystalline Gd$_2$NiMnO$_6$ samples, Murthy *et al.* reported ferromagnetism with a Curie temperature $T_c \approx 130$ K, while Oh *et al.* observed the Griffiths phase above ferromagnetic (FM) ordering temperature [10,11]. Apart from mixed valency and ASD, the R-site cation also influences magnetism through $3d$-$4f$ and $4f$-$4f$ exchange interaction (at low temperature), which leads to antiferromagnetic (AFM) ordering giving rise to large magnetic entropy change particularly in R_2NiMnO$_6$ DP systems [6,11,12]. The cooling of a magnetic material is achieved when exposed to a varying magnetic field due to isothermal magnetic entropy change (ΔS_M), popularly known as magnetocaloric effect (MCE). MCE can be efficiently utilized in magnetic refrigeration technology without any environmental hazards [13]. Among various oxides such as rare-earth manganites, cobaltates, and spinel ferrites [13], rare-earth based DPs have emerged to be a prototype system for tuning the MCE [7,12,14,15]. Subtle change in orbital and spin orderings influence ΔS_M as well as relative cooling power (RCP) significantly. The cooling capacity of a magnetic refrigerant is defined by RCP $= -\Delta S_M^{\max} \times \delta T_{\mathrm{FWHM}}$, where $-\Delta S_M^{\max}$

*amitava@iitk.ac.in
†sudipta@iitgoa.ac.in
‡chanchal@iitk.ac.in

and δT_{FWHM} represent the maximum entropy change and the width of $-\Delta S_M$ vs T curve, respectively. Particularly, in La$_2$MiMnO$_6$ single crystals, $-\Delta S_M$ is found to be 3 J Kg^{-1} K^{-1} with a field change of 7 T along with a wider transition width (hence high RCP) [16]. Another single crystal work on R_2CoMnO$_6$ finds large anisotropic nature in MCE owing to the strong magnetocrystalline anisotropy [2,14]. The magnetic easy axis of the rare-earth and transition metal networks can be different, which makes this topic even more intriguing [2,14].

Physical properties, especially magnetism in DPs, can be highly influenced by appropriate growth conditions in thin films. In particular strain, oxygen stoichiometry, fluence, and growth temperature control the structure, magnetism, and transport properties [15,18,19]. Most of the DP thin films are grown using pulsed laser deposition (PLD). Strain can influence the B-site octehedral distortion which controls the $90°$ nearest neighbor and $180°$ next nearest neighbor superexchange interactions. Recent works on LNMO thin films grown on (100)-oriented SrTiO$_3$ (STO) and LaSrAlO$_4$ substrates reveal a structural change owing to tensile and compressive strains, respectively [20]. This also induces ferroelectricity in LNMO thin films grown on STO (111) [21] as the tensile strain displaces the La^{+3} cation along the (111) direction giving rise to polar nature. The saturation magnetization in LNMO thin films can also be tuned via in-plane strain [22]. The FM T_c is enhanced in Y$_2$NiMnO$_6$ thin films by tensile strain [23]. A variation in strain from -1.1% (compressive) to 0.58% (tensile) rotates the easy axis of magnetization from out-of-plane to in-plane in Sr$_2$FeMoO$_6$ thin films [24]. On the other hand, MCE in thin films can be altered by tuning shape anisotropy, strain-induced anisotropy, and magnetocrystalline anisotropy. However, there is a lack of study in this regard, particularly in DP thin films. A recent report by Matte *et al.* suggests that ΔS_M can be tuned by appropriate thin film growth conditions [15].

To find the true magnetic ground state and the effect of strain on magnetism, a comprehensive thin film study in R_2NiMnO$_6$ is necessary. In addition, the anisotropy study in R_2NiMnO$_6$ thin films is important for tuning MCE. With these issues in mind, we have studied the structural, magnetic, and magnetocaloric properties of Gd$_2$NiMnO$_6$ (GNMO) thin films grown on the SrTiO$_3$ (001). In particular, the evolution of structure, magnetism, magnetic anisotropy, and MCE is studied with thickness in GNMO. The magnetic ground state and magnetic anisotropy is also studied using density functional theory (DFT) calculations.

II. EXPERIMENTAL DETAILS

We have grown thin films of GNMO using PLD technique (KrF excimer laser, Lambda Physik COMPex Pro, $\lambda = 248$ nm). STO substrate was cleaned using NH$_4$HF solution as described by Ghising *et al.* to obtain the TiO$_2$ terminated STO surface [25]. The deposition was carried out at laser frequency 5 Hz and substrate temperature 800 °C in an oxygen environment (0.2 mbar). Before deposition, the substrates were annealed for half an hour at 800 °C. After deposition, the samples were *in situ* annealed at 600 °C for 1 h. Thin films of GNMO with thickness 15 nm (S-15), 40 nm (S-40), and 60 nm

(S-60) were grown on STO substrates. The thin film x-ray diffraction (XRD) was carried out in a PANalytical X'pert PRO diffractometer using the Cu-K_α source of wavelength 1.5405 Å. The thickness measurement was done using x-ray reflectivity (XRR). The valencies of the constituent elements were probed by x-ray photoelectron spectroscopy (XPS) using a PHI 5000 Versa Prob II (FEI Inc.) system. The magnetization measurements were performed using a superconducting quantum interference device (SQUID) magnetometer (Quantum Design, USA).

III. CALCULATION METHODOLOGY

The density-functional theory (DFT) calculations were performed within the plane-wave basis set based on the pseudopotential framework as implemented in the Vienna *ab initio* simulation package (VASP) [26,27]. The generalized gradient approximation (GGA) exchange-correlation functional was employed following the Perdew-Burke-Ernzerhof prescription [28]. The experimentally obtained structures were optimized by relaxing the atomic positions towards equilibrium until the Hellmann-Feynman force becomes less than 0.001 eV/Å, keeping the lattice parameters fixed at their experimentally obtained values. In order to incorporate correlations beyond the scope of GGA, Hubbard U was introduced by performing GGA+U calculations [29,30] with suitable values of $U_{\text{eff}} = 5$ eV (U-J_H) at the Mn and Ni sites. The effect of spin orbit coupling (SOC) is introduced as a scalar relativistic correction term to the Hamiltonian to understand its interplay with other existing energy scales. The calculations were performed with a plane wave cut-off of 500 eV and $4 \times 4 \times 2$ k mesh in the Brillouin zone was used for self-consistent calculations.

IV. RESULTS AND DISCUSSIONS

A. Structural characterization

Figure 1(a) shows the three dimensional crystal structure of GNMO generated from refined powder XRD data. GNMO crystallizes in the $P2_1/n$ space group with monoclinic crystal structure. The transition-metal elements (Ni and Mn) occupy 2d and 2c Wyckoff sites in a rock-salt type arrangement and the rare-earth element (Gd) takes the 4e Wyckoff site (intermediate space between the NiO$_6$ and MnO$_6$ octahedra). Figure 1(b) shows the θ-2θ XRD scan of GNMO films. All three samples show only (00l) reflections indicating the highly c-axis oriented growth. Figure 1(c) represents the rocking curves for all three samples with a spread of mosaicity from $0.3°$ to $1.1°$. A careful look [Fig. 1(b)] at the (002) plane of the θ-2θ XRD scan reveals that the thinnest sample S-15 has a slightly higher c-axis lattice parameter (3.84 Å) than that of the thickest sample, S-60 (3.815 Å). The bulk c-axis lattice parameter of pseudocubic GNMO is reported to be 3.783 Å [11]. The cubic STO substrate has lattice mismatch of 3.12% with bulk GNMO, which indicates the possibility of strain evolution at the GNMO/STO interface. It is evident from Fig. 1(d) [zoom-in view of (002) peaks] that there are two stable crystallographic phases, GNMO(002)$_{P1}$ and GNMO-(002)$_{P2}$. P1 corresponds to strained phase and P2 to strain-relaxed phase. The c-axis lattice parameter decreases
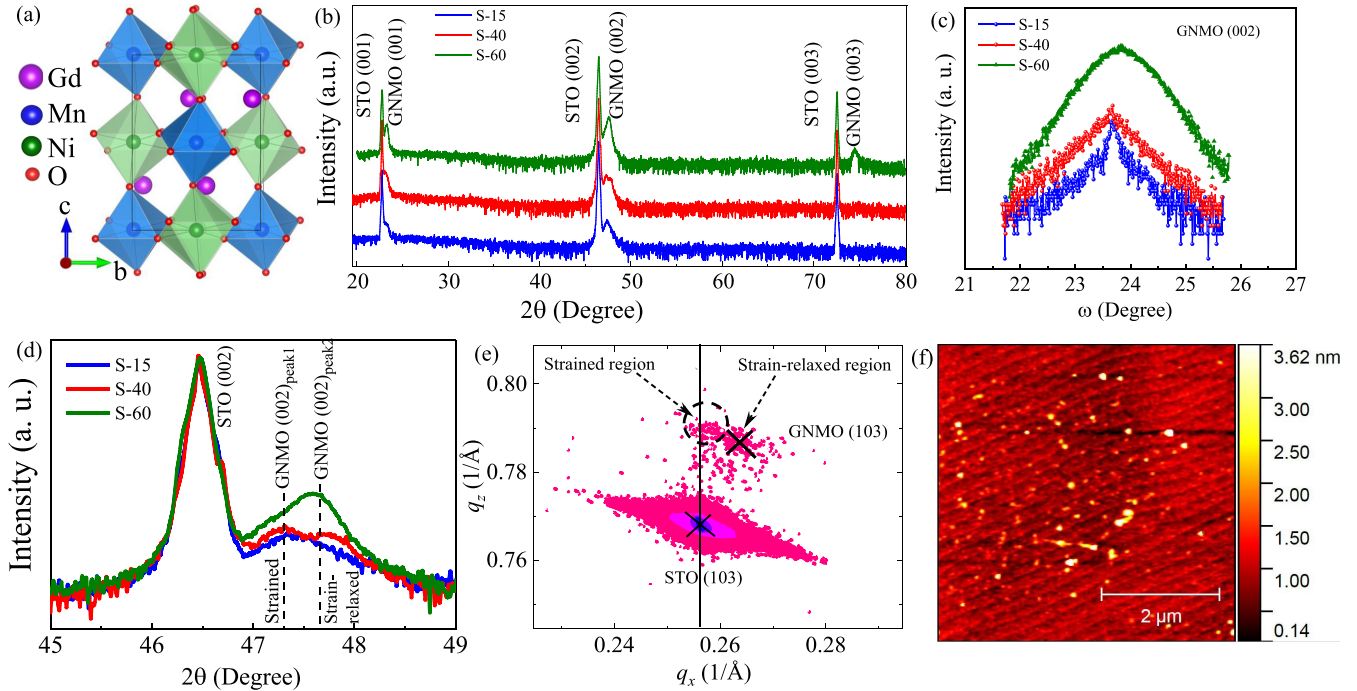
FIG. 1. Structural characterization of Gd$_2$NiMnO$_6$ (GNMO) thin films: (a) 3D monoclinic crystallographic unit cell of GNMO compound obtained from VESTA software [17], (b) XRD pattern (θ-2θ scan) of S-15, S-40, and S-60 thin films, (c) rocking curves (ω scan) for all three samples at (002) plane, (d) zoomed-in view of θ-2θ scan around (002) plane, (e) reciprocal space map of S-40, and (f) AFM image of S-15.

with rising thickness. The existence of interfacial strain is clearly visible from the reciprocal space mapping (RSM) of S-40 in the vicinity of a (103) reflection peak of STO as shown in Fig. 1(e). The coexistence of both GNMO(002)$_{P1}$ and GNMO(002)$_{P2}$ is depicted by the dotted circle and crossed regions around the pseudocubic (103) plane of GNMO, respectively. The in-plane (a-axis) lattice parameters of P1 and P2 are 3.903 Å and 3.798 Å, respectively. Since the in-plane lattice parameter of the substrate (3.905 Å) is larger than that of the sample (3.783 Å), the in-plane strain ought to be tensile in nature. The values of this tensile strain along the a-axis direction are found to be 3.17% and 0.4% for GNMO(002)$_{P1}$ and GNMO(002)$_{P2}$, respectively. Clearly, P1 gets stronger as the thickness increases, indicating that thinner samples have more strained phases and thicker samples have larger volume fraction of strain-relaxed phases. The surface morphology of the S-15 thin film is shown in Fig. 1(f). The rms roughness of S-15 is 0.45 nm. The surface topography of S-15 depicts an atomic step-terrace-like pattern, which is a representative of two-dimensional growth.

B. X-ray photoelectron spectroscopy

Figure 2 depicts the room temperature XPS spectra of S-60 for Gd, Ni, Mn, and O, respectively. The XPS survey scan confirmed the presence of all the elements without any impurity peak. The oxidation states were calculated using an asymmetric Gauss-Lorentz sum function along with a linear background fit with the help of XPS PEAKFIT4.1 software. The Gd-4d core-level spectra consists of two peaks, Gd-4$d_{5/2}$ ($\sim$141.7 eV) and Gd-4$d_{3/2}$ ($\sim$146.6 eV), as shown in Fig. 2(a). The binding energy of these peaks confirms the

Gd^{+3} oxidation state [31,32]. In Fig. 2(b), the deconvoluted Mn-2p core level spectra contains two main characteristic peaks 2$p_{3/2}$ ($\sim$642.3 eV) and 2$p_{1/2}$ ($\sim$654.2 eV). This confirms the +4 oxidation states of the Mn ion [33–35]. The Ni-2p core-level spectra shown in Fig. 2(c) is comprised of
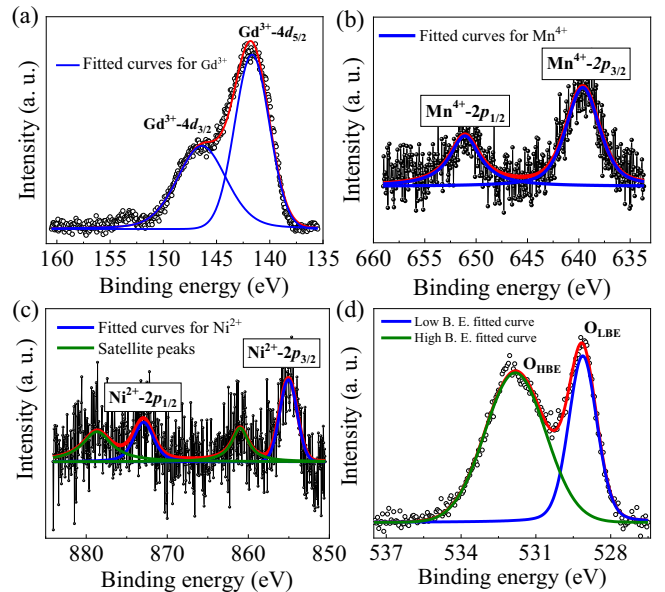

FIG. 2. Deconvoluted core-level XPS spectra for different constituent elements in S-60 thin film: (a) Gd-4d spectra, (b) Mn-2p spectra, (c) Ni-2p spectra, and (d) O-1s spectra. Red solid line represents the fitted curve.
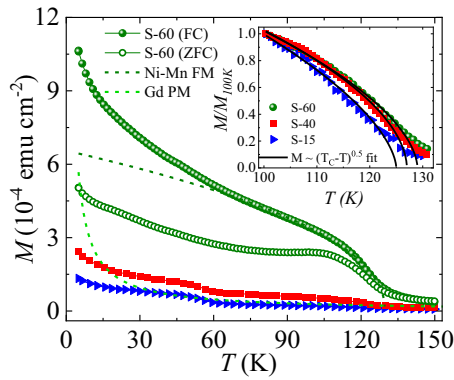
FIG. 3. Field-cooled (FC) magnetization (solid symbol) and zero-field-cooled (ZFC) magnetization (open symbol) measured with an in-plane magnetic field of 0.1 T for GNMO thin films. The dotted olive-green line and dotted green line correspond to individual contributions of Ni-Mn and Gd for S-60. The normalized data with mean-field critical power law fit is shown in the inset.

Ni-$2p_{3/2}$ ($\sim$855.2 eV) and Ni-$2p_{1/2}$ ($\sim$872.9 eV) peaks revealing the presence of only Ni^{2+} ions in the system [36]. The other two peaks are termed as satellite peaks for Ni^{2+} [36]. The O-1s spectrum shown in Fig. 2(d) exhibits two peaks, O$_{LBE}$ ($\sim$529.1 eV) and O$_{HBE}$ ($\sim$531.9 eV). O$_{LBE}$ and O$_{HBE}$ peaks correspond to the O^{2-} (metal-oxygen bond) [37] and hydroxyl (OH$^-$) or carbonate (CO$_3$$^{2-}$) anion adsorbed on the top surface of GNMO [33].

C. Magnetic properties

Figure 3 represents the field-cooled (FC) in-plane ($H \parallel ab$) M-T data for all three samples and zero-field-cooled (ZFC) data for S-60 measured at 0.1 T. A sharp change is evident around 129 K for S-60, which corresponds to the ferrimagnetic (FEM) T_c. The value of T_c was determined by fitting the mean-field critical power law (inset of Fig. 3), $M = M_0(T_c\text{-}T)^{0.5}$, in the vicinity of the critical region. A decrease in T_c is noticed in the lower thickness samples ($T_c = 125$ K for S-15 and $T_c = 127$ K for S-40). The decrease in T_c in GNMO thin films is due to the finite size effect [38] and strain [22]. The bulk T_c in GNMO is reported to be 132 K [10]. In addition, a sharp rise in M-T is also observed below 20 K, which can be attributed to the large paramagnetic (PM) contribution from rare-earth Gd. The small change in magnetization (S-15 and S-40) around 55 K has extrinsic origin (oxygen peak) [39]. The FC-ZFC splitting in M-T curves of S-60 below T_c indicates the presence of magnetocrystalline anisotropy. Ferrimagnetism in GNMO is ascribed to the dominant superexchange interaction between Mn^{+4} and Ni^{+2} cations mediated by the O^{-2} anion and the process is governed by the Goodenough-Kanamori rule [40,41]. To visualize the origin of the magnetic ground state more clearly, we have evaluated the magnetization contribution due to Gd and Ni-Mn separately as demonstrated in Fig. 3. The PM and FEM contributions arise from the Gd^{+3}-O-Gd^{+3} and Ni^{+2}-O-Mn^{+4} superexchange interactions, respectively. However, the non-saturating magnetic hysteresis (shown later) suggests that the Ni-Mn exchange is antiferromagnetic with two magnetic sub-
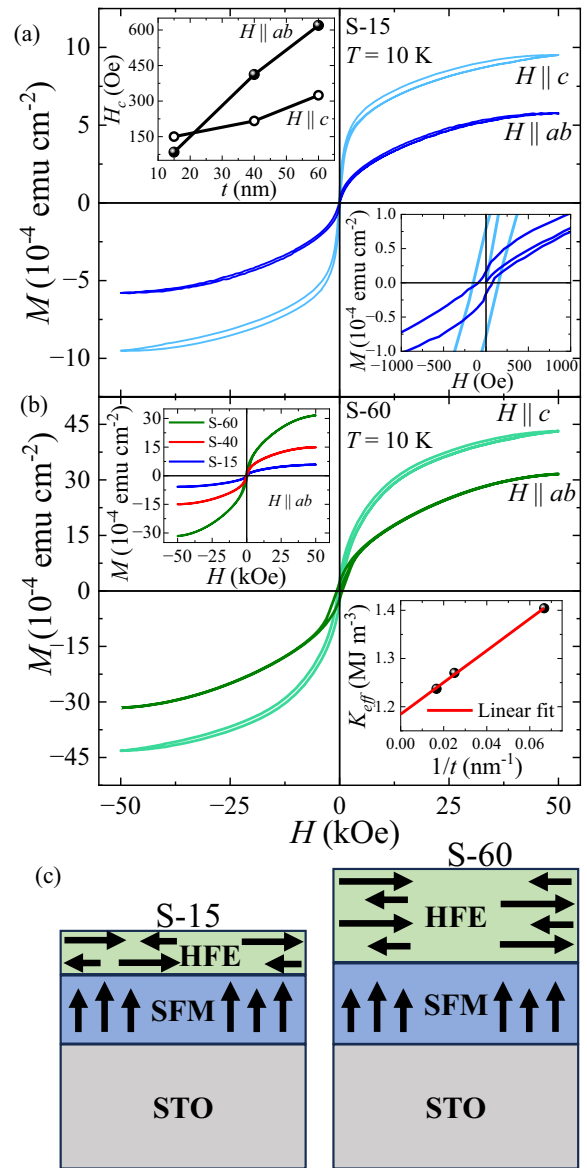

FIG. 4. (a) In-plane (*ab* plane) and out-of-plane (*c* plane) magnetic hysteresis recorded at 10 K for S-15. Lower inset is the zoomed-in view around the low-field region. Upper inset shows the evolution of in-plane and out-of-plane coercivity with thickness and (b) in-plane and out-of-plane magnetic hysteresis for S-60 recorded at 10 K. The upper inset of (b) shows the comparative plot of in-plane hysteresis at various thickness. The lower inset shows the estimated anisotropy constant vs inverse of thickness and (c) schematic picture of S-15 and S-60 showing the possible evolution of SFM and HFE.

lattices of unequal moments leading to ferrimagnetism. This is also clarified by theoretical calculations (Sec. IV D).

Further, for more insight about the magnetic ground state as well as magnetic anisotropy, M-H hysteresis data was recorded at low temperature (10 K) with magnetic field along both in-plane ($H\parallel ab$) and out-of-plane ($H\parallel c$) directions. Figures 4(a) and 4(b) show the M-H data for S-15 and S-60, respectively. It is evident from Fig. 4(a) that out-of-plane (OP) is the easy axis for S-15 and S-60 indicating perpendicular magnetic anisotropy (PMA) in GNMO. A very careful

look at the OP hysteresis of Fig. 4(a) reveals that the low field region has minimal opening in the hysteresis whereas, in the high field, it exhibits much more opening. This peculiar shape of the hysteresis indicates the interplay among various anisotropies in the system. The in-plane (IP) data shows significantly reduced magnetization than the OP data. Generally, the easy axis lies along the IP direction due to the inherent shape anisotropy of thin films. Thus the occurrence of PMA in GNMO films is intriguing. Magnetic anisotropy in these samples can be analyzed in terms of mixed anisotropies due to combination of soft ferromagnet (SFM) and a hard ferrimagnet (HFE) phases. The SFM has PMA and it can be associated with the strained structure, while the HFE is associated with the strain-relaxed structure as discussed in Sec. IV A. Figure 4(b) shows the M-H hysteresis for S-60. The OP direction is still the easy axis of magnetization, but the difference between the OP and IP magnetization has reduced significantly compared to S-15. The OP hysteresis has nearly uniform opening up to high field. This suggests that HFE is dominant over SFM for S-60. The low-field susceptibility can be calculated from the low-field slope of IP or OP hysteresis. At all thickness, the OP susceptibilities are larger than the IP susceptibilities, which is evident from the sharp rise of the OP hysteresis curve in the zoomed in view [bottom inset of Fig. 4(a)]. The evolution of SFM and HFE with thickness can be further understood from the coercive field (H_c) vs thickness plot [as seen in top inset of Fig. 4(a)]. The IP H_c increases sharply ($\sim$6 times) with thickness compared to the gradually increasing (around 2 times) OP H_c. The evolution of magnetism with thickness depicts that SFM remains nearly constant while the HFE phase increases with thickness as depicted in the schematic of Fig. 4(c). This is consistent with our earlier proposition about the SFM being associated to the strained phase. Overall, the PMA decreases with increasing thickness. In order to quantify the PMA, we have estimated the effective anisotropy constant

$$K_{\text{eff}} = K_{\perp} + K_{\text{sh}}. \quad (1)$$

$K_{\perp}$ carries the contribution from magnetocrystalline and strain-induced anisotropies, whereas K_{sh} corresponds to shape anisotropy [42]. $K_{\perp}$ can be estimated from the area difference between IP and OP hysteresis curves and $K_{\text{sh}} = -\frac{1}{2}\mu_0 M_S^2$, where M_S is the saturation magnetization along the easy direction. The value of $K_{\perp}$ decreases from 1.15 MJ m^{-3} for S-15 to 0.9 MJ m^{-3} for S-60. The change in the value of $K_{\perp}$ with thickness is related to the strain-induced anisotropy in the background of magnetocrystalline anisotropy. The estimated values of K_{sh} turn out to be -335 KJ m^{-3} and -253 KJ m^{-3} for S-15 and S-60, respectively. In thin films, K_{eff} can be expressed as a function of thickness (t) as

$$K_{\text{eff}} = K_v + \frac{K_{S_1} + K_{S_2}}{t}. \quad (2)$$

Here K_v is the bulk (magnetocrystalline) anisotropy and K_{S_1}, K_{S_2} are the surface anisotropies at the top and bottom surfaces of the GNMO layer [43]. $K_{S_1} + K_{S_2}$ and K_v can be evaluated from the slope and intercept obtained after linear fitting the K_{eff} vs $1/t$ data as shown in the bottom inset of Fig. 4(b). For any material exhibiting PMA, this slope should

TABLE I. Comparison of anisotropy constant.

Sample	K_{eff} (15 nm)	K_{eff} (60 nm)	$K_{S_1}+K_{S_2}$	K_v
GNMO	1.4 MJ m^{-3}	1.23 MJ m^{-3}	3.2 mJ m^{-2}	1.184 MJ m^{-3}
LCMO	1.64 MJ m^{-3}	1.16 MJ m^{-3}	9.18 mJ m^{-2}	1.02 MJ m^{-3}

be positive. We find the slope $K_{S_1} + K_{S_2} = 3.2$ mJ m^{-2} and intercept $K_v = 1.184$ MJ m^{-3}. Table I gives a comparison of K_{eff} and $K_{S_1} + K_{S_2}$ for GNMO and La$_2$CoMnO$_{6-\epsilon}$ (LCMO) [44] thin films. The LCMO thin films also exhibit PMA. The order of magnitudes of K_{eff} and $K_{S_1} + K_{S_2}$ for GNMO films match very well with LCMO films. Thickness tuning of PMA can be very useful for various spintronic applications [45].

D. Electronic structure calculation

In order to understand the above experimental results from the microscopic point of view, we have performed DFT based first principles calculation for the bulk as well as thin-film structures of Gd$_2$NiMnO$_6$. Due to the presence of two 3d elements, the incorporation of the Hubbard U parameter was essential to take care of the strong electronic correlation. The DFT calculations were also performed with varied parameters of Hubbard U and various possible spin configurations of the magnetic sites. The orbital projected GGA+U ($U_{\text{eff}} = 5$ eV) spin polarized density of states (DOS) for the bulk structure is shown in Fig. 5. We find that a band gap opens up at the Fermi energy level, even in the absence of the Hubbard U, and this band gap is further enhanced with the inclusion of U, which suggests that the material falls under the category of a typical Mott insulator. From the Gd-f DOS [Fig. 5(a)], we find that it is completely filled in one spin channel, whereas the other spin channel is completely empty and lies 3 eV away from the E_f. In Fig. 5(b), Mn-t_{2g} states (blue curve) are empty in the majority spin channel and completely filled in the minority spin channel, whereas the Mn-e_g states (cyan curve) are completely empty in both the spin channels. On the other hand, the Ni-t_{2g} states (light-green curve) are completely filled in both the spin channels and the Ni-e_g (dark-green curve) states are filled only in the majority spin channel as shown in Fig. 5(c). The completely empty Ni-e_g minority spin channel lies around 4 eV away from the E_f. The calculated spin magnetic moment at the Gd site is 6.84μ_B. At the Mn site we find a spin moment of $-3.10\mu_B$, whereas at the Ni site the value obtained is 1.73μ_B. The point to be noted here is that the Mn spin moments are antiparallel to that of the Ni spin moments, even if we started with the initial parallel configuration, which suggests that there is a strong AFM interaction between the Mn and Ni sublattices. The induced magnetic moment at the oxygen site is negligible and is of the order of 0.08μ_B/site. With the change in the value of U_{eff} from 0 to 6 eV, we find that the magnetic moment at the Gd site remains unchanged, while that of Mn and Ni sites vary from (-2.55 to $-3.23\mu_B$) and (1.44 to 1.78μ_B), respectively. The total magnetic moment however remains constant at 13 μ_B per formula unit. From the above findings we can conclude that Gd is in a $+3$ ($4f^7$) electronic state with a high spin state of $S = \frac{7}{2}$, Mn is in a $+4$ ($3d^3$) electronic state with an intermediate spin state
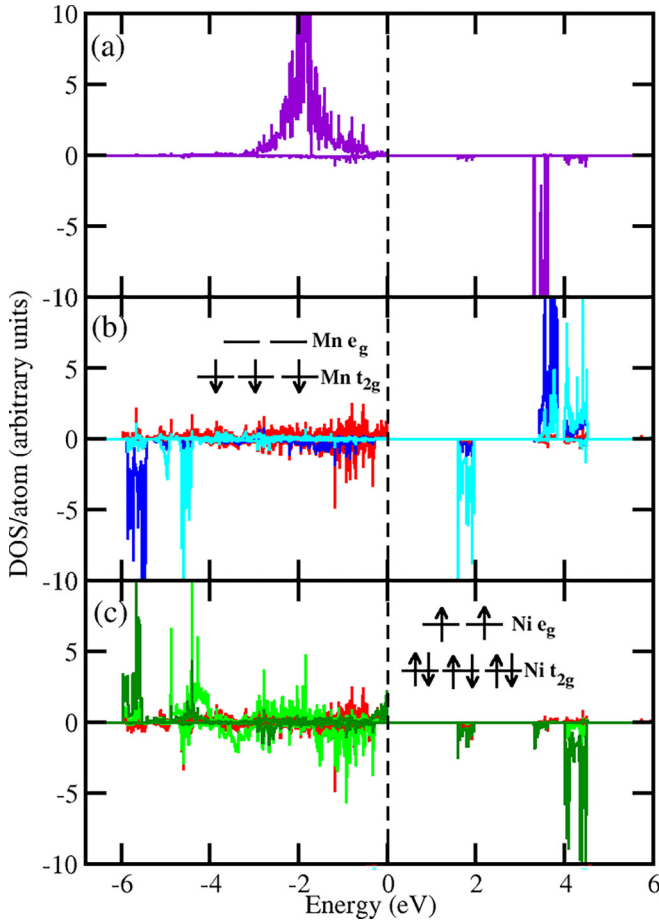
FIG. 5. Calculated GGA+U orbital projected density of states for Gd_2NiMnO_6. (a) Density of states for Gd-f (violet curve), (b) density of states for Mn-t_{2g}, Mn-e_g states, and O-$2p$ states represented by blue, cyan, and red curves, respectively, and (c) density of states for Ni-t_{2g}, Ni-e_g states and O-$2p$ states represented by light green, dark green, and red curves respectively. The distribution of electrons for the Mn-d and Ni-d states has been shown in (b) and (c), respectively. The Fermi energy is set at zero in the energy scale.

FIG. 6. Ground state spin configurations obtained from DFT calculations for Gd_2NiMnO_6 in (a) bulk Structure and (b) strained structure. The violet, blue, and green atoms represent Gd, Mn, and Ni atoms, respectively. Red and yellow arrows depict the two possible spin orientations. The dotted unit cell represents bulk unit cell indicating volume expansion in strained unit cell, (c) hard-ferrimagnetic phase for strain-relaxed structure, and (d) soft ferromagnetic phase for strained structure with arrows scaled to moment magnitudes. Since the Gd ordering takes place below 10 K, the magnetic contribution of Gd atoms is neglected.

$S = \frac{3}{2}$, and Ni is in a $+2$ ($3d^8$) electronic state with a low spin state of $S = 1$. The above findings are consistent with the experimental results.

Further, to understand the magnetic ground state of Gd_2NiMnO_6, we performed total energy calculations for various possible spin configurations of the system. Figure 6 pictorially depicts the ground state magnetic configurations. Our calculations reflect that the configuration depicted in Fig. 6(a) is the lowest energy magnetic ground state of the bulk structure system. The total energy of this particular configuration [Fig. 6(a)] is $\approx$3 eV lower than the others. In this particular case, the intrasublattices interactions of Gd, Mn, and Ni are of FM type whereas, for the intersublattices, Gd spins align ferromagnetically with Ni and antiferromagnetically with Mn. The interaction between Mn and Ni is thus AFM in nature. FM and AFM interactions among different magnetic sublattices result in an overall ferrimagnetic system with the uncompensated magnetic moment. These theoretical calculations for bulk (strain-relaxed) structure qualitatively match with the experimental results. Experimentally, the
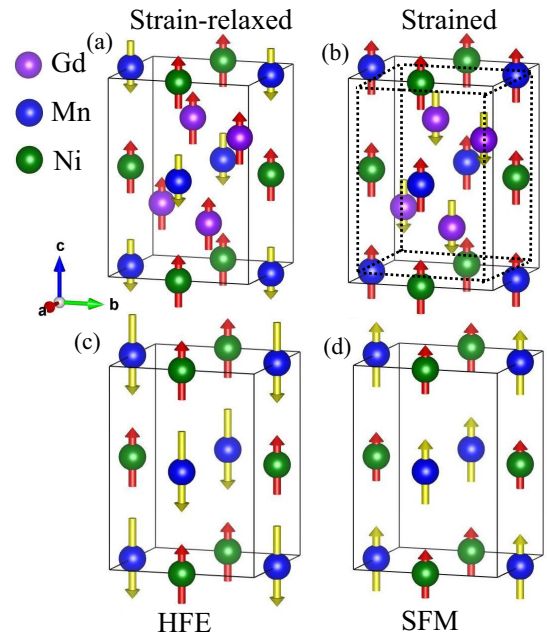
shape of the hysteresis as well as the nonsaturating tendency [S-60, Fig. 4(b)] indicate the hard-ferrrimagnetic ground state of the system as depicted in Fig. 6(c).

In order to correspond the electronic structure results with experimental findings obtained on thin films, we also performed electronic structure calculations on strained lattice structure of Gd_2NiMnO_6, which is equivalent to that of thin films of Gd_2NiMnO_6. Due to structural modification, the band structure of the thin film undergoes changes as reflected in Fig. 7. The major noticeable difference in the band structure is the change in the band gap. In the strained structure, which is equivalently mimicking the material in the thin film condition, the band gap decreases due to the major change in the conduction band. In the strained structure of Gd_2NiMnO_6, the conduction band is pushed down towards the Fermi energy in both the spin channels. As a result of the change in the band dispersion, the details of the electron hopping gets modified compared to that of the bulk Gd_2NiMnO_6. The magnetic moment at the Gd, Mn, and Ni sites changes to $6.84\mu_B$, $-2.00\mu_B$, and $1.03\mu_B$, respectively. The electronic occupation and the total magnetic moment of the system however remains unchanged. The variation in magnetic moment at the Mn site compared to the bulk case (from -3.10 to $-2.0\mu_B$) gets compensated by a converse change in moment at the Ni site (from 1.73 to $1.03\mu_B$). Hence the total magnetic moment per formula unit remains constant at $13\mu_B$. There is however modification in the magnetic ground state of the system when we move
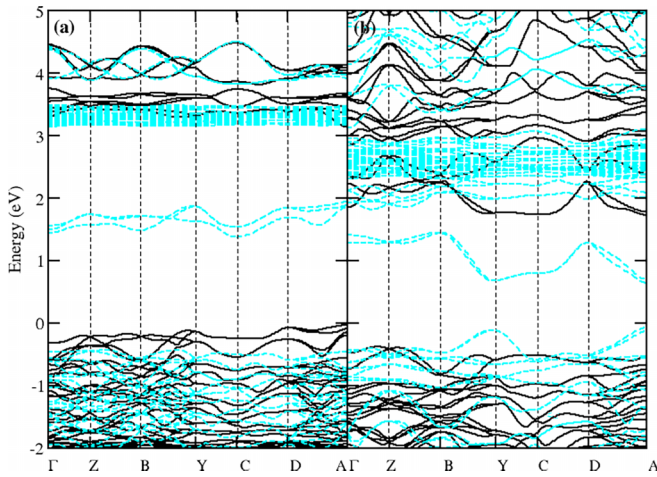
FIG. 7. Calculated GGA+U electronic band structure is shown for Gd_2NiMnO_6 for (a) bulk structure and (b) strained lattice structure. The black and turquoise curves represent the band structure for the majority and minority spin channels, respectively. The Fermi energy is set at zero in the energy scale.

from the bulk to strained structure as shown in Fig. 6(b). In the strained structure, while the spins in the intrasublattices of Gd, Mn, and Ni are aligned FM, the interaction between Gd-Mn and Gd-Ni intersublattice is AFM in nature. Unlike the bulk case, the Mn-Ni sublattice is FM in nature. This supports our previous proposition of soft FM [Fig. 6(d)] and AFM (HFE) in strained and strain-relaxed (bulk) structures, respectively, in GNMO.

To understand the effect of SOC, we also performed GGA+U+SOC calculations for the bulk structure. The ground state magnetic configuration was considered in the above case. There are minimal changes in the spin magnetic moment at the Gd, Ni, and Mn sites on the inclusion of SOC. The orbital magnetic moment is negligible at the Gd and Mn sites. At the Ni site, however, there is a minimal orbital magnetic moment along the direction of the spin magnetic moment which is of the order of $\approx -0.1\mu_B$. Further inspections involving setting the quantization axis along various directions [viz. (001), (100), (010), (110), (101), and (111)] aid us in concluding that the global easy axis for the bulk structure is along the (001) direction. The point to be noted here is that only the Gd spins align exactly in the (001) direction. The magnetic moment at the Mn and Ni sites are distributed along all the crystallographic axes, even in the lowest energy configuration. This further suggests the possibility of a canting of spins and a noncollinear magnetic structure. However, due to a large moment at the Gd site, the spin ordering takes place at low temperature. In the case of strained structure, the easy axis has changed to the (100) direction. Additionally, the calculated value of the magnetocrystalline anisotropy (MCA) energy is very high in the bulk structure, while there is a drastic reduction of MCA energy in the strained structure. The anisotropy constant $K_\perp$ (containing contribution from both MCA and strain-induced anisotropy) decreases with increasing thickness, which is opposite to the MCA trend. This can be true only when the strain-induced anisotropy outweighs the MCA in the strained structure. Thus the large value of $K_\perp$ in S-15

is predominantly due to the strain-induced anisotropy. In S-60 (bulklike), MCA is dominant over strain induced anisotropy. Thus our theoretically calculated easy axis (001) matches with experimental results for the bulk structure (S-60).

E. Magnetocaloric effect

The ordering of the Ni^{+2}-O-Mn^{+4} spins across the PM-FM transition and Gd^{+3} spins at low temperature is associated with large change in magnetic entropy of the GNMO system. The net change in magnetic entropy ($-\Delta S_M$) can be estimated from a set of isothermal magnetization (*M-H* isotherm) data. Figures 8(a) and 8(d) show *M-H* isotherms recorded from 10 K to 100 K with an interval of 10 K for S-60 for IP and OP, respectively. $-\Delta S_M$ is calculated with a magnetic field change from 0 to H using the well-known Maxwell thermodynamic relation:

$$-\Delta S_M = \int_0^H \frac{M(T + \Delta T, H) - M(T, H)}{\Delta T} dH. \quad (3)$$

The anisotropy in MCE is studied in detail for S-60. Figures 8(b) and 8(e) display the variation of $-\Delta S_M$ as a function of temperature in low temperature for both IP and OP directions, respectively. The sharp rise in $-\Delta S_M$ below 20 K for both IP and OP is due to the Gd^{+3} ordering as discussed in the earlier sections. For both IP and OP, $-\Delta S_M$ shows a sharp decrease up to 20 K owing to the PM Gd. The small hump-like feature around 55 K is of extrinsic origin (oxygen) as discussed in the magnetization section. Interestingly, the OP $-\Delta S_M$ is found to be two times smaller than the IP value. It is evident from the theoretical calculation that the Gd^{+3} ions are predominantly oriented along the *c* axis. The presence of such single-ion anisotropy results in a direction dependent $-\Delta S_M$ in thin film GNMO [Fig. 8(c)]. Similar anisotropic character of MCE has been observed in Gd_2CoMnO_6 and Tb_2CoMnO_6 single crystals, where both Gd^{+3} and Tb^{+3} have a tendency to align along the *ab* plane but MCE is higher along the *c* axis [2,14]. The field-dependent magnetic entropy change can be represented in terms of the following power law: $-\Delta S_M \sim H^n$ [53]. All three curves of Fig. 8(c) exhibit concave upward curvature fitted with this empirical power law. The value of the exponent (n) for in-plane magnetic entropy change is higher (1.7) than that of the out-of-plane (1.4) at 11 K. These values of n suggest that the magnetic transition is likely to be first order type rather than second order [54,55]. In order to calculate RCP, we have measured $-\Delta S_M^{max}$ in the vicinity of Ni-Mn ordering. $|\Delta S_M^{max}|$ and RCP are found to be 1.4 J Kg^{-1} K^{-1} and 75 J Kg^{-1} for $\Delta H = 5$ T. The field dependence of RCP can be expressed by a scaling relation: RCP $\propto H^{1+\frac{1}{\delta}}$ [56]. The RCP vs H plot [inset of Fig. 8(c)] is well fitted with critical exponent $\delta = 3.125$. Such value of δ suggests the spin-spin interaction to be mean-field-like. Further study reveals that the improved crystalline orientation and quality enhances the magnetocaloric effect as seen in Fig. 8(c). The IP $-\Delta S_M$ of S-60 shows 90% enhancement compared to the polycrystalline GNMO (11.41 J Kg^{-1} K^{-1}). The obtained values of $|\Delta S_M^{max}|$ are much larger than similar types (Ni-Mn and Co-Mn) of DP systems [2,6,10,14]. This is further indicated by the red filled circle in Fig. 8(f), which compares the $-\Delta S_M$ values of various R_2BMnO_6 (B = Ni, Co, Zn, Cr, Cu) DPs in polycrys-
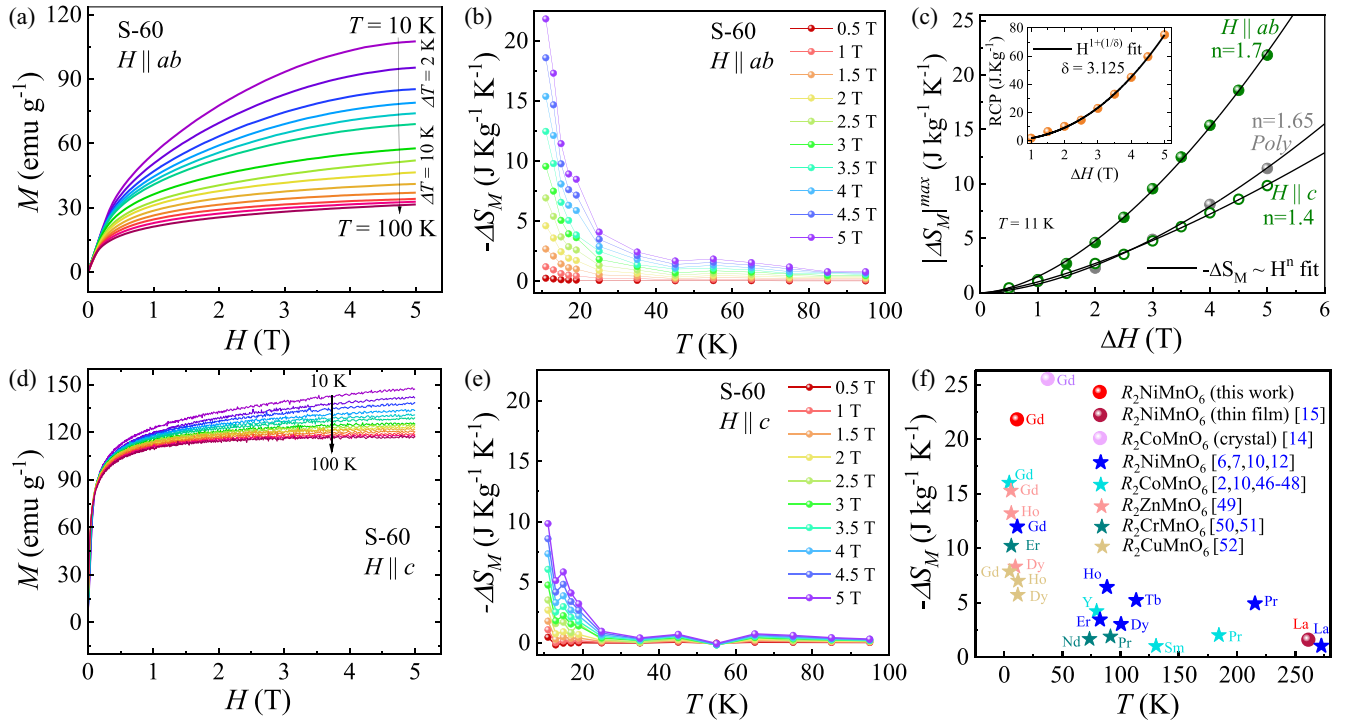
FIG. 8. (a) In-plane *M-H* isotherms for S-60 recorded at various temperatures as stated in the graph, (b) in-plane $-\Delta S_M$ as a function of temperature for various fields, and (c) in-plane and out-of-plane $|\Delta S_M^{max}|$ as a function of magnetic fields for S-60 in comparison with reported polycrystalline GNMO [10]. The black lines correspond to power-law fitting by $-\Delta S_M \propto H^n$. Inset shows the variation of RCP vs field change across Ni-Mn magnetic ordering at 129 K, (d) out-of-plane *M-H* isotherms recorded at various temperatures as stated in the graph, (e) out-of-plane $-\Delta S_M$ as a function of temperature for various fields, and (f) comparison plot of $-\Delta S_M$ as a function of temperature in R_2BMnO$_6$ family of double perovskite compounds studied in literature [2,6,7,10,12,15,46–52], where B = Ni, Co, Zn, Cr, and Cu. Here, solid symbols correspond to thin films and single crystals and star marks indicate the polycrystalline form of the materials.

talline, single crystal, and thin film forms [2,6,7,10,12,15,46–52]. The use of smaller rare-earth atoms (such as Gd, Ho) at the *R* site gives giant magnetocaloric effect [2,10,54]. It is evident that the compounds with a *B*-Mn combination of Ni-Mn and Co-Mn possess the higher $-\Delta S_M$.

V. CONCLUSION

We have successfully grown high quality *c*-axis oriented thin films of GNMO on STO (001) substrates. The XPS studies combined with DOS calculations confirm the presence of Mn^{+4} intermediate spin state and Ni^{+2} low spin state in the samples. The XRD and magnetic measurement data reveals an evolution of two distinct crystallographic phases: the "strained" phase associated to a soft ferromagnetic phase and the "strain-relaxed" phase associated with a hard-ferrimagnetic phase. Our theoretical calculations also suggest that the relative spin orientation of Mn and Ni changes from antiparallel to parallel configuration with increasing strain.

The tensile strain installs perpendicular magnetic anisotropy in GNMO. The epitaxial nature and *c*-axis oriented GNMO results in significant enhancement in MCE. Further, the MCE is found to be large and anisotropic in nature. The entropy change along OP is half of that along IP ($|\Delta S_{M_{max}}| = 21.82$ J Kg^{-1} K^{-1} at $T = 11$ K for $H||ab$). The giant value of $-\Delta S_M$ establishes GNMO as a prospective candidate for magnetic refrigeration. This work opens up the possibility of increasing the values of ΔS_M significantly in some of the other DP thin films (especially Gd, Ho, Er, and Dy based) compared to their bulk counterparts. For future work, the role of compressive as well as tensile strain in tuning ΔS_M will be interesting from both theoretical and experimental perspectives.

[1] D. Serrate, J. M. De Teresa, and M. R. Ibarra, Double perovskites with ferromagnetism above room temperature, J. Phys.: Condens. Matter **19**, 023201 (2006).

[2] J. Y. Moon, M. K. Kim, D. G. Oh, J. H. Kim, H. J. Shin, Y. J. Choi, and N. Lee, Anisotropic magnetic properties and giant rotating magnetocaloric effect in double-perovskite Tb$_2$CoMnO$_6$, Phys. Rev. B **98**, 174424 (2018).

[3] D. Choudhury, P. Mandal, R. Mathieu, A. Hazarika, S. Rajan, A. Sundaresan, U. V. Waghmare, R. Knut, O. Karis, P. Nordblad *et al.*, Near-room-temperature colossal magnetodielectricity and multiglass properties in partially disordered La_2NiMnO_6, Phys. Rev. Lett. **108**, 127201 (2012).

[4] S. Vasala and M. Karppinen, $A_2B'B''O_6$ perovskites: a review, Prog. Solid State Chem. **43**, 1 (2015).

[5] M. K. Kim, J. Y. Moon, H. Y. Choi, S. H. Oh, N. Lee, and Y. J. Choi, Investigation of the magnetic properties in double perovskite R_2CoMnO_6 single crystals (R= rare earth: La to Lu), J. Phys.: Condens. Matter **27**, 426002 (2015).

[6] Y. Jia, Q. Wang, Y. Qi, and L. Li, Multiple magnetic phase transitions and magnetocaloric effect in double perovskites R_2NiMnO_6 (R= Dy, Ho, and Er), J. Alloys Compd. **726**, 1132 (2017).

[7] T. Chakraborty, H. Nhalil, R. Yadav, A. A. Wagh, and S. Elizabeth, Magnetocaloric properties of R_2NiMnO_6 (R= Pr, Nd, Tb, Ho and Y) double perovskite family, J. Magn. Magn. Mater. **428**, 59 (2017).

[8] S. Pal, S. Jana, S. Govinda, B. Pal, S. Mukherjee, S. Keshavarz, D. Thonig, Y. Kvashnin, M. Pereiro, R. Mathieu *et al.*, Peculiar magnetic states in the double perovskite Nd_2NiMnO_6, Phys. Rev. B **100**, 045122 (2019).

[9] A. K. Singh, S. Chauhan, S. K. Srivastava, and R. Chandra, Influence of antisite disorders on the magnetic properties of double perovskite Nd_2NiMnO_6, Solid State Commun. **242**, 74 (2016).

[10] J. K. Murthy, K. D. Chandrasekhar, S. Mahana, D. Topwal, and A. Venimadhav, Giant magnetocaloric effect in Gd_2NiMnO_6 and Gd_2CoMnO_6 ferromagnetic insulators, J. Phys. D: Appl. Phys. **48**, 355001 (2015).

[11] S. H. Oh, H. Y. Choi, J. Y. Moon, M. K. Kim, Y. Jo, N. Lee, and Y. J. Choi, Nonlinear magnetodielectric effect in double-perovskite Gd_2NiMnO_6, J. Phys. D: Appl. Phys. **48**, 445001 (2015).

[12] K. P. Shinde, E. J. Lee, M. Manawan, A. Lee, S.-Y. Park, Y. Jo, K. Ku, J. M. Kim, and J. S. Park, Structural, magnetic, and magnetocaloric properties of R_2NiMnO_6 (R= Eu, Gd, Tb), Sci. Rep. **11**, 20206 (2021).

[13] N. R. Ram, M. Prakash, U. Naresh, N. S. Kumar, T. S. Sarmash, T. Subbarao, R. J. Kumar, G. R. Kumar, and K. C. B. Naidu, Review on magnetocaloric effect and materials, J. Supercond. Nov. Magn. **31**, 1971 (2018).

[14] J. Y. Moon, M. K. Kim, Y. J. Choi, and N. Lee, Giant anisotropic magnetocaloric effect in double-perovskite Gd_2CoMnO_6 single crystals, Sci. Rep. **7**, 16099 (2017).

[15] D. Matte, M. de Lafontaine, A. Ouellet, M. Balli, and P. Fournier, Tailoring the magnetocaloric effect in La_2NiMnO_6 thin films, Phys. Rev. Appl. **9**, 054042 (2018).

[16] M. Balli, P. Fournier, S. Jandl, and M. M. Gospodinov, A study of the phase transition and magnetocaloric effect in multiferroic La_2MnNiO_6 single crystals, J. Appl. Phys. **115**, 173904 (2014).

[17] K. Momma and F. Izumi, VESTA 3 for three-dimensional visualization of crystal, volumetric and morphology data, J. Appl. Crystallogr. **41**, 1272 (2008).

[18] S. Majumder, M. Tripathi, R. Raghunathan, P. Rajput, S. N. Jha, D. O. de Souza, L. Olivi, S. Chowdhury, R. J. Choudhary, and D. M. Phase, Mapping the magnetic state as a function of antisite disorder in Sm_2NiMnO_6 double perovskite thin films, Phys. Rev. B **105**, 024408 (2022).

[19] N. Kumar, R. Gupta, R. Kaur, D. Oka, S. Kakkar, S. Kumar, S. Singh, T. Fukumura, C. Bera, and S. Chakraverty, B-site stoichiometry control of the magnetotransport properties of epitaxial Sr_2FeMoO_6 thin film, ACS Appl. Electron. Mater. **3**, 597 (2021).

[20] X. W. Jin, L. Lu, S. B. Mi, M. Liu, and C. L. Jia, Phase stability and b-site ordering in La_2NiMnO_6 thin films, Appl. Phys. Lett. **109**, 031904 (2016).

[21] R. Takahashi, I. Ohkubo, K. Yamauchi, M. Kitamura, Y. Sakurai, M. Oshima, T. Oguchi, Y. Cho, and M. Lippmaa, A-site-driven ferroelectricity in strained ferromagnetic La_2NiMnO_6 thin films, Phys. Rev. B **91**, 134107 (2015).

[22] D. Kumar and D. Kaur, Structural and magnetic properties of La_2NiMnO_6 thin films on $LaAlO_3$ substrate with varying thickness, J. Alloys Compd. **554**, 277 (2013).

[23] C. Xie and L. Shi, Tuning of magnetic properties for epitaxial Y_2NiMnO_6 thin film:substrate is crucial, Appl. Surf. Sci. **384**, 459 (2016).

[24] C. Du, R. Adur, H. Wang, A. J. Hauser, F. Yang, and P. C. Hammel, Control of magnetocrystalline anisotropy by epitaxial strain in double perovskite Sr_2FeMoO_6 films, Phys. Rev. Lett. **110**, 147204 (2013).

[25] P. Ghising and Z. Hossain, Electric field control of the photoinduced resistance increase in $La_0.7Sr_0.3MnO_3/LaTiO_3/SrTiO_3$ heterostructure, Phys. Rev. B **100**, 115119 (2019).

[26] G. Kresse and J. Hafner, *Ab-initio* molecular dynamics for liquid metals, Phys. Rev. B **47**, 558(R) (1993).

[27] G. Kresse and J. Furthmüller, Efficient iterative schemes for *ab-initio* total-energy calculations using a plane-wave basis set, Phys. Rev. B **54**, 11169 (1996).

[28] J. P. Perdew, K. Burke, and M. Ernzerhof, Generalized gradient approximation made simple, Phys. Rev. Lett. **77**, 3865 (1996).

[29] V. I. Anisimov, I. V. Solovyev, M. A. Korotin, M. T. Czyżyk, and G. A. Sawatzky, Density-functional theory and NiO photoemission spectra, Phys. Rev. B **48**, 16929 (1993).

[30] S. L. Dudarev, G. A. Botton, S. Y. Savrasov, C. J. Humphreys, and A. P. Sutton, Electron-energy-loss spectra and the structural stability of nickel oxide: An LSDA+ U study, Phys. Rev. B **57**, 1505 (1998).

[31] N. Zhang, D. Chen, F. Niu, S. Wang, L. Qin, and Y. Huang, Enhanced visible light photocatalytic activity of Gd-doped $BiFeO_3$ nanoparticles and mechanism insight, Sci. Rep. **6**, 26467 (2016).

[32] A. Kumar, A. Kumar, and A. Kumar, Energy storage properties of double perovskites Gd_2NiMnO_6 for electrochemical supercapacitor application, Solid State Sci. **105**, 106252 (2020).

[33] R. X. Silva, R. M. Almeida, R. L. Moreira, R. Paniago, M. V. S. Rezende, and C. W. A. Paschoal, Vibrational properties and infrared dielectric features of Gd_2CoMnO_6 and Y_2CoMnO_6 double perovskites, Ceram. Int. **45**, 4756 (2019).

[34] R. X. Silva, R. L. Moreira, R. M. Almeida, R. Paniago, and C. W. A. Paschoal, Intrinsic dielectric properties of magnetodielectric La_2CoMnO_6, J. Appl. Phys. **117**, 214105 (2015).

[35] J. Su, Z. Z. Yang, X. M. Lu, J. T. Zhang, L. Gu, C. J. Lu, Q. C. Li, J.-M. Liu, and J. S. Zhu, Magnetism-driven ferroelectricity in double perovskite Y_2NiMnO_6, ACS Appl. Mater. Interfaces **7**, 13260 (2015).

[36] H. W. Nesbitt, D. Legrand, and G. M. Bancroft, Interpretation of Ni2p XPS spectra of Ni conductors and Ni insulators, Phys. Chem. Miner. **27**, 357 (2000).

[37] B. Ghosh and S. Mukhopadhyay, Unified description of resistivity and thermopower of $Pr_2Ir_2O_7$: Possible influence of crystal field excitation in a kondo lattice, Phys. Rev. B **103**, 165135 (2021).

[38] R. Zhang and R. F. Willis, Thickness-dependent Curie temperatures of ultrathin magnetic films: effect of the range of spin-spin interactions, Phys. Rev. Lett. **86**, 2665 (2001).

[39] M. Vrankić, A. Šarić, S. Bosnar, D. Pajić, J. Dragović, A. Altomare, A. Falcicchio, J. Popović, M. Jurić, M. Petravić *et al.*, Magnetic oxygen stored in quasi-1d form within $BaAl_2O_4$ lattice, Sci. Rep. **9**, 15158 (2019).

[40] J. B. Goodenough, Theory of the role of covalence in the perovskite-type manganites [La, M(II)]MnO_3, Phys. Rev. **100**, 564 (1955).

[41] J. Kanamori, Superexchange interaction and symmetry properties of electron orbitals, J. Phys. Chem. Solids **10**, 87 (1959).

[42] F. Eskandari, S. B. Porter, M. Venkatesan, P. Kameli, K. Rode, and J. M. D. Coey, Magnetization and anisotropy of cobalt ferrite thin films, Phys. Rev. Mater. **1**, 074413 (2017).

[43] M. T. Johnson, P. J. H. Bloemen, F. J. A. Den Broeder, and J. J. De Vries, Magnetic anisotropy in metallic multilayers, Rep. Prog. Phys. **59**, 1409 (1996).

[44] R. Galceran, L. López-Mir, B. Bozzo, J. Cisneros-Fernández, J. Santiso, L. Balcells, C. Frontera, and B. Martínez, Strain-induced perpendicular magnetic anisotropy in La_2CoMnO_6 thin films and its dependence on film thickness, Phys. Rev. B **93**, 144417 (2016).

[45] B. Dieny and M. Chshiev, Perpendicular magnetic anisotropy at transition metal/oxide interfaces and applications, Rev. Mod. Phys. **89**, 025008 (2017).

[46] C. L. Li, L. G. Wang, X. X. Li, C. M. Zhu, R. Zhang, H. W. Wang, and S. L. Yuan, Magnetic field-induced metamagnetism and magnetocaloric effect in double perovskites Re_2CoMnO_6 (Re= Sm, Dy), Mater. Chem. Phys. **202**, 76 (2017).

[47] Y. Jia, X. Zhang, Z. Zhang, and L. Li, Effect of sintering temperature on microstructure and magnetic properties of double perovskite Y_2CoMnO_6, Ceram. Int. **44**, 19794 (2018).

[48] K. Rawat, Meenakshi, and R. N. Mahato, Investigation of structural, magnetic, and magnetocaloric properties of nanocrystalline double perovskite Pr_2CoMnO_6, Mater. Res. Express **5**, 066110 (2018).

[49] L. Li, P. Xu, S. Ye, Y. Li, G. Liu, D. Huo, and M. Yan, Magnetic properties and excellent cryogenic magnetocaloric performances in b-site ordered RE_2ZnMnO_6 (RE = Gd, Dy and Ho) perovskites, Acta Mater. **194**, 354 (2020).

[50] B. Wu, D. Guo, Y. Wang, and Y. Zhang, Crystal structure, magnetic properties, and magnetocaloric effect in B-site disordered RE_2CrMnO_6 (RE = Ho and Er) perovskites, Ceram. Int. **46**, 11988 (2020).

[51] Y. Jia, Y. Cheng, H. Wang, Z. Zhang, and L. Li, Magnetocaloric properties and critical behavior in double perovskite RE_2CrMnO_6 (RE = La, Pr, and Nd) compounds, Ceram. Int. **46**, 25043 (2020).

[52] Y. Zhang, B. Zhang, S. Li, J. Zhu, B. Wu, J. Wang, and Z. Ren, Cryogenic magnetic properties and magnetocaloric effects (MCE) in B-site disordered RE_2CuMnO_6 (RE = Gd, Dy, Ho and Er) double perovskites (DP) compounds, Ceram. Int. **47**, 18205 (2021).

[53] H. Oesterreicher and F. T. Parker, Magnetic cooling near curie temperatures above 300 K, J. Appl. Phys. **55**, 4334 (1984).

[54] K. P. Patra and S. Ravi, Re-entrant spin glass and magnetocaloric effect in frustrated double perovskite Ho_2CoMnO_6 flat nanorod, J. Magn. Magn. Mater. **559**, 169537 (2022).

[55] J. Y. Law, V. Franco, L. M. Moreno-Ramírez, A. Conde, D. Y. Karpenkov, I. Radulov, K. P. Skokov, and O. Gutfleisch, A quantitative criterion for determining the order of magnetic phase transitions using the magnetocaloric effect, Nat. Commun. **9**, 2680 (2018).

[56] R. C. Sahoo, S. Das, and T. K. Nath, Influence of magnetic frustration and structural disorder on magnetocaloric effect and magneto-transport properties in $La_{1.5}Ca_{0.5}CoMnO_6$ double perovskite, J. Appl. Phys. **123**, 013902 (2018).